


Carrier concentration independent plasmons in biased twisted bilayer graphene

Ma Zhou 

BAQIS, Beijing Academy of Quantum Information Sciences, P.O. Box 912, Beijing 100083, China
and SKLSM, Institute of Semiconductors, Chinese Academy of Sciences, P.O. Box 912, Beijing 100083, China



(Received 10 May 2021; accepted 8 July 2021; published 20 July 2021)

We calculate the density-density response function of biased twisted bilayer graphene (BTBG) and study its plasmon dispersion within the random phase approximation (RPA). At long wavelengths ($q \rightarrow 0$), plasmon dispersion shows local classical behavior $\omega = \omega_0 \sqrt{q}$. Unlike the situation in conventional two-dimensional electron gas (2DEG), where the density dependence of the plasmon energy is of the form $\omega_0 \propto \sqrt{n}$ (n is the carrier concentration), the plasmon energy ω_0 is independent of the carrier concentration (n) in biased twisted bilayer graphene. Furthermore, the plasmon energy (ω_0) is also independent of the Fermi energy (μ) which is decided by the carrier concentration (n).

DOI: [10.1103/PhysRevB.104.045419](https://doi.org/10.1103/PhysRevB.104.045419)

I. INTRODUCTION

The dynamical dielectric function and collective density oscillations (plasmons) of an interacting electron gas are of fundamental interest from both an experimental and theoretical perspective. Many theoretical [1–3] and experimental [4,5] studies on the dielectric function of various two-dimensional (2D) systems have been made in the past years. The 2D plasmon dispersion relation was first derived by Ritchie [6] and by Ferrell [7] who were treating the characteristic energy loss of electrons in metal foils. In 1967, the response of a two-dimensional electron gas (2DEG) to a longitudinal electric field of arbitrary wave vector and frequency was calculated in the self-consistent-field approximation by Stern [8]. In 1975, 2D plasmons and electron-ripplon scattering in a sheet of electrons on liquid helium was observed by Grimes and Adams [9]. The 2D plasmons have also been experimentally observed in different kinds of 2D systems such as a quantum well [10,11] and metal film [12–16].

Since the discovery of graphene in 2004, the experimental fabrication of different atomic monolayers has been a subject of great interest [17]. The plasmons in 2D monolayer materials have attracted the attention of many researchers. In 2007, the dynamical dielectric function $\epsilon(\omega, q)$ of 2D graphene at an arbitrary wave vector q and frequency ω was calculated within the random phase approximation (RPA) by Hwang and Das Sarma [18]. They concluded that at long wavelengths $q \rightarrow 0$, the plasmon dispersion showed local classical behavior $\omega = \omega_0 \sqrt{q}$, but the density dependence of the plasma frequency $\omega_0 \propto n^{1/4}$ was different from the usual 2D electron system $\omega_0 \propto n^{1/2}$ [9]. In 2010, this special density dependence of the plasmon frequency was confirmed experimentally by Brar [19].

Although, there are many different 2D systems (quantum well, graphene, monolayer MoS₂, and so on), the long-wavelength 2D plasmon spectrum can be described by the same formula $\omega \propto \sqrt{\mu} \sqrt{q}$ for different 2D materials [20,21]. Therefore, a higher Fermi energy μ will generate a higher plasmon energy at the same plasmonic wavelength.

The recent discovery of correlated insulation and seemingly unconventional superconductivity in twisted bilayer graphene (TBG) has revived interest in TBG [22]. Importantly, these phenomena are observed in a narrow range of twist angles near 1.05°, i.e., the first magic angle where the isolated and relatively flat bands appear near neutrality [23]. Besides superconductivity, the dielectric property for small twist angle bilayer graphene has also attracted much attention from both an experimental [24] and theoretical [25–28] perspective. In 2017, Hu and Fei measured the plasmon energy in TBG and found that the plasmon spectrum under a long-wavelength limit still depends on the Fermi energy (μ) as a form $\omega \propto \sqrt{\mu} \sqrt{q}$ [24]. In 2019, Lewandowska and Levitova theoretically studied the plasmon spectrum for small twist angle TBG [27]. They obtained that the mode dispersion has a square-root form characteristic of 2D plasmons $\omega \propto \sqrt{\beta_q} \sqrt{q}$ with a weak q dependence in β_q . However, the leading order of β_q was still determined by the Fermi energy μ .

Here, we investigate the dynamical dielectric function of biased twisted bilayer graphene (BTBG) in a wide range of twist angles $\theta > 2^\circ$. We find that the perpendicular electric field can remove the degeneration of the graphene Dirac cone and give rise to a Dirac energy difference Δ_z between the two Dirac points at the same valley. When the Fermi energy μ is located in the regime ($\mu < \Delta_z/2$), the real part of the polarization function ($\text{Re}[\Pi(q \rightarrow 0, \omega)] = q^2/(2\pi\omega^2)\Delta_z$) is independent of the specific value of the Fermi energy μ . Furthermore, this Fermi energy (μ) irrelative polarization function [$\Pi(q \rightarrow 0, \omega)$] leads to a carrier concentration (n) independent plasmon spectrum, $\omega \propto \omega_0 \sqrt{q} \propto \sqrt{\Delta_z} \sqrt{q}$, which also indicates that the plasmon energy (ω_0) is determined by the Dirac energy deviation (Δ_z).

The rest of this paper is organized as follows. In Sec. II, we introduce the effective Hamiltonian for BTBG which can well describe the double Dirac cone band structure. In Sec. III A, we adopt the Lindhard model to calculate the long-wavelength polarization function $\Pi(q \rightarrow 0^+, \omega)$ of the BTBG by using our effective Hamiltonian, and obtain the Fermi energy

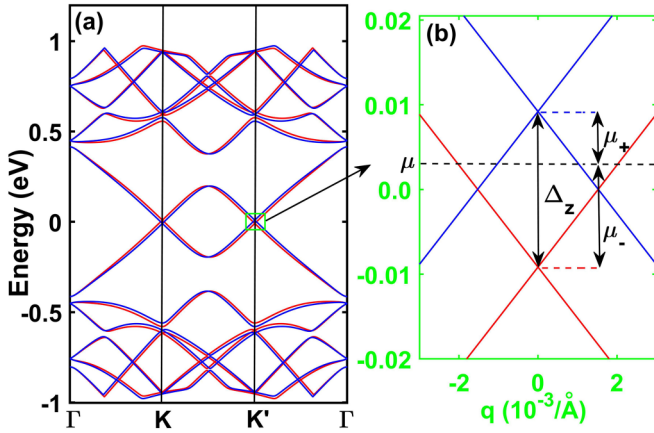


FIG. 1. (a) Energy dispersion for the bands closest to the Dirac point plotted along the k -space trajectory $\Gamma \rightarrow K \rightarrow K' \rightarrow \Gamma$ for $\theta = 3.89^\circ$, under a bias voltage $V_b = 12$ mV. (b) The enlarged plot of the Dirac cone in the green box. Δ_z is Dirac energy deviation induced by bias voltage V_b . μ is the Fermi energy which can be tuned by electron or hole doping.

independent plasmon spectrum. In Sec. III B, by using RPA, we calculate the polarization function $\Pi(q, \omega)$ in the whole (q, ω) regime, and reconfirm the Fermi energy independent plasmon spectrum at a long-wavelength limit. We perform further calculations to study the energy loss function and plasmon spectrum of BTBG in the whole regime. In Sec. III C, we discuss the impact of the finite-range interaction. The summary and final conclusions are in Sec. IV.

II. EFFECTIVE HAMILTONIAN FOR BIASED TWISTED BILAYER GRAPHENE

Based on the well-known effective continuum model [29], we calculate the moiré bands as a function of their Brillouin-zone momentum k for BTBG by using the plane wave expansion. The results for the bias voltage $V_b = 12$ mV, and twist angle $\theta = 3.89^\circ$ are shown in Fig. 1(a). Figure 1(b) is the enlarged plot of the green box region indicated in Fig. 1(a), where the Dirac cones are deviated about Δ_z eV due to the bias voltage (V_b). The blue line and red line represent the energy bands of $\xi = \pm$ valleys, respectively. They are the time reversal partners of each other. As we can see in Fig. 1, the Dirac cones of a single-layer graphene remain present in the bilayer, but with a significant reduction of the Fermi velocity. It is worth noting that the Dirac cones present in the bilayer with a twist are essentially the Dirac cones of each layer perturbed by the admixture of states of the opposing layer, which are distant in energy. Since there is no coupling between the red ($\xi = +1$) and blue ($\xi = -1$) bands, a bias voltage V_b should only amount to a relative shift of the energies of the degeneracy points in each cone. This can be clearly seen in Fig. 1(b), where the Dirac cones of different valley index $\xi = \pm$ deviate from each other but there is no gap in the spectrum. Therefore, we define a Dirac cone deviation energy Δ_z [shown in Fig. 1(b)] to describe the bias voltage effect.

Based on the effective Hamiltonian of BTBG created by Santos [30], we can numerically fit a Hamiltonian to describe the bias voltage effect on the electronic structure near the K

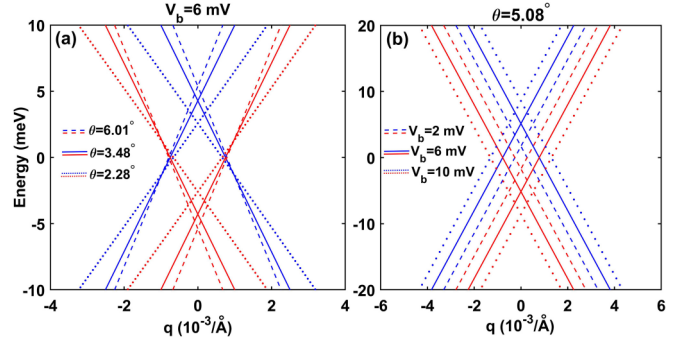


FIG. 2. (a) Plane wave expansion calculated band structure near the K' point for different twist angles $\theta = 6.01^\circ$ (dashed), $\theta = 3.48^\circ$ (solid), and $\theta = 2.28^\circ$ (dotted). The bias voltage is $V_b = 6$ mV for all different angles. (b) Band structure near the K' point for different bias voltages $V_b = 2$ mV (dashed), $V_b = 6$ mV (solid), and $V_b = 10$ mV (dotted). The twist angle is $\theta = 5.08^\circ$ for all different bias voltages. The red (blue) lines represent the $\xi = +1$ ($\xi = -1$) valley contributed band structure.

and K' points. We calculate the band structure near the K' points of different twist angles and bias voltages, and display the results in Figs. 2(a) and 2(b). As we can see in Fig. 2(a), for a specific bias voltage ($V_b = 6$ mV), the Fermi velocity and Dirac deviation energy Δ_z increase when the twist angles increase from 2.28° (dotted lines) to 6.01° (dashed lines). Figure 2(b) indicates that, for a specific twist angle, although the Dirac deviation Δ_z increases, the Fermi velocity does not change, when the bias voltage increases from 2 to 6 mV. According to the results shown in Fig. 2, we conclude that Δ_z is a function of bias voltage V_b and twist angle θ . On the other hand, the Fermi velocity $v(\theta)$ only relies on the twist angle. After a tedious and straightforward numerical fitting, we obtain a low-energy Hamiltonian to describe the deviated band structure near the K (K') points,

$$\mathbf{H} = v(\theta)[k_x \sigma_x + k_y \sigma_y] + \tau \xi \frac{\Delta_z}{2},$$

$$\Delta_z = [v(\theta)\alpha + \beta]V_b, \quad (1)$$

where $\alpha = 0.6115/\text{\AA}$, $\beta = -0.6409(e)$, and

$$v(\theta) = 0.0079\theta^4 - 0.0943\theta^3 + 0.4536\theta^2 - 0.6877\theta + 1.8407. \quad (2)$$

In this model Hamiltonian [Eq. (1)], σ_x and σ_y stand for the Pauli matrix, and $\tau = +1$ (-1) for the K (K') valley shown in Fig. 1(a). The $\xi = +1$ (-1) represents the corresponding monolayer graphene valley index. Equation (1) shows that Dirac deviation energy Δ_z is linearly reliant on the bias voltage V_b for a specific twist angle. On the other hand, the relation between the twist angle and Fermi velocity is complicated. Here, we obtain Eq. (2) to describe the θ dependent Fermi velocity $v(\theta)$ by numerical fitting.

At small twist angles $\theta < 2^\circ$, the relaxed lattice drastically reduces the area of the AA stacking region and forms a triangular domain structure with alternating AB and BA stacking regions [26,31]. Since the bias voltage V_b can open an electronic gap in the Bernal AB or BA stacked regions, the bias voltage will generate a band gap when the twist angle is

small ($\theta < 2^\circ$). Therefore, we only use Hamiltonian Eq. (1) to study the dielectric properties of BTBG when the twist angle is located in the range $\theta > 2^\circ$.

III. DIELECTRIC FUNCTION AND PLASMON

Many physical properties rely on the dynamical dielectric function $\epsilon(\omega, q)$. This function has been studied extensively in a variety of 2D systems beyond the usual electron gas. In the random phase approximation (RPA), the dielectric function $\epsilon(\omega, q)$ is given by [8]

$$\epsilon(\omega, q) = 1 - V(q)\Pi(\omega, q). \quad (3)$$

Here, $V(q) = \frac{e^2}{2\epsilon_0\epsilon_r q}$ is the Fourier transform of the Coulomb potential in two dimensions, $V(r) = \frac{e^2}{4\pi\epsilon_0\epsilon_r r}$, ϵ_0 the vacuum permittivity, and $\epsilon_r = 1$ for the free-standing material. In this paper all the numerical results are calculated by $\epsilon_r = 1$ unless the ϵ_r have been redefined. Equation (3) contains the free polarizability given by a two-dimensional integral in momentum space [20],

$$\begin{aligned} \Pi(q, \omega) = g_s \sum_{\kappa\kappa'} \int \frac{d^2k}{(2\pi)^2} & | \langle \Psi_{\kappa}(\mathbf{k}) | \Psi_{\kappa'}(\mathbf{k} + \mathbf{q}) \rangle |^2 \\ & \times \frac{f[E_{\kappa}(\mathbf{k})] - f[E_{\kappa'}(\mathbf{k} + \mathbf{q})]}{\omega - E_{\kappa'}(\mathbf{k} + \mathbf{q}) + E_{\kappa}(\mathbf{k}) + i0^+}. \end{aligned} \quad (4)$$

$|\Psi_{\kappa/\kappa'}(\mathbf{k})\rangle$ and $E_{\kappa/\kappa'}(\mathbf{k})$ are the eigenstates and energies, κ and κ' denote the band indices, and $g_s = 2$ stands for spin degeneracy. Here, we work at zero temperature so that the Fermi functions $f[E_{\kappa}(\mathbf{k})]$ and $f[E_{\kappa'}(\mathbf{k} + \mathbf{q})]$ can be replaced by step functions.

A. Lindhard results

When we study the long-wavelength intraband polarization function $\Pi(q \rightarrow 0, \omega)$, Eq. (4) can be simplified into a Lindhard model:

$$\Pi(q, \omega) = \int \frac{d^2k}{(2\pi)^2} \frac{f[E(\mathbf{k})] - f[E(\mathbf{k} + \mathbf{q})]}{\omega - E(\mathbf{k} + \mathbf{q}) + E(\mathbf{k}) + i0^+}. \quad (5)$$

By using the Lindhard model Eq. (5), we can analytically obtain the long-wavelength intraband plasmon spectrum.

Since the band structure of BTBG has particle-hole symmetry, the corresponding dielectric properties for the hole doping case ($\mu < 0$) and the electron doping case ($\mu > 0$) are identical. Here, we only study the dielectric properties for the electron doping case ($\mu > 0$). For convenience, we define $\mu_+ = |\mu - \Delta_z/2|$ ($\mu_- = |\mu + \Delta_z/2|$) to represent the energy distance between the Fermi energy and the upper (lower) deviated Dirac point, as shown in Fig. 1(b). It is worth noting that there is no coupling between the red ($\xi = +1$) and blue ($\xi = -1$) bands. Therefore, we can respectively obtain the polarization function of μ_+ and μ_- as below (details of the

deduced steps are shown in the Appendix):

$$\begin{aligned} \text{Re}[\Pi(q \rightarrow 0^+, \omega)] &= \frac{q^2}{4\pi\omega^2}(\mu_+ + \mu_-) \\ &= \begin{cases} \frac{q^2}{4\pi\omega^2}\Delta_z & : \mu < \frac{\Delta_z}{2}, \\ \frac{q^2}{2\pi\omega^2}\mu & : \mu > \frac{\Delta_z}{2}. \end{cases} \end{aligned} \quad (6)$$

The plasmon branch can be obtained by finding the zeros of the dielectric function $\epsilon(q, \omega)$ [Eq. (1)]. In the regime where $\text{Im}[\Pi(q, \omega)] = 0$, it is sufficient to solve

$$1 = \frac{e^2}{2\epsilon_0\epsilon_r q} \text{Re}[\Pi(q, \omega)]. \quad (7)$$

By substituting Eq. (6) into Eq. (7), we obtain the long-wavelength plasmon branch,

$$\omega = \omega_0\sqrt{q} = \begin{cases} \sqrt{\frac{e^2}{8\pi\epsilon_0\epsilon_r}}\sqrt{\Delta_z}\sqrt{q} & : \mu < \frac{\Delta_z}{2}, \\ \sqrt{\frac{e^2}{4\pi\epsilon_0\epsilon_r}}\sqrt{\mu}\sqrt{q} & : \mu > \frac{\Delta_z}{2}. \end{cases} \quad (8)$$

Based on Eq. (8), we conclude that the plasmon dispersion does not rely on carrier concentration, when the corresponding Fermi energy $\mu < \Delta_z/2$. Since the dependence between carrier concentration and Fermi energy is of the form $\mu = \sqrt{(\pi v^2/2)n - (\Delta_z/2)^2}$, the relation between the plasmon energy and carrier concentration is $\omega_0 \propto [(\pi v^2/2)n - (\Delta_z/2)^2]^{1/4}$, when the Fermi energy is located in the regime $\mu > \Delta_z/2$.

Conventional plasmonics emerged from the early study of 2DEG, where free electrons oscillate collectively in resonance with the electromagnetic field. In graphene, plasmon excitation can be performed by using a radiation (frequency range from terahertz to midinfrared), where the wave vector of the incident electromagnetic wave can match that of the 2D graphene plasmon. Since the electromagnetic radiation has a frequency $\omega = c\hbar q$, for BTBG, the energy of radiation induced plasmon mode has a simple form:

$$E_{\text{ph}} = \begin{cases} \frac{e^2}{8\pi c\epsilon_0\epsilon_r}\Delta_z & : \mu < \frac{\Delta_z}{2}, \\ \frac{e^2}{4\pi c\epsilon_0\epsilon_r}\mu & : \mu > \frac{\Delta_z}{2}. \end{cases} \quad (9)$$

According to Eq. (9), we conclude that the radiation excited plasmon energy (E_{ph}) linearly relies on Δ_z , when the Fermi energy is located in the regime $\mu < \Delta_z/2$. On the other hand, the plasmon energy (E_{ph}) linearly relies on the Fermi energy (μ), when the Fermi energy is located in the regime ($\mu > \Delta_z/2$).

B. Random phase approximation results

The above analysis for BTBG dielectric properties is based on the Lindhard model without taking the interband contributions into consideration. For a long-wavelength $q \rightarrow 0^+$ and low-frequency situation, results obtained by using the Lindhard model can describe the dielectric properties very well. However, in order to study the dielectric properties in a shorter-wavelength and higher-frequency regime, we need to recalculate the polarization function by using the RPA equation [Eq. (4)]. Since the polarization function depends on the value of the $\mu_+ = |\mu - \Delta_z/2|$ and $\mu_- = |\mu + \Delta_z/2|$, which we have already defined, we present the polarization

results as a function of μ_+ and μ_- . Equation (4) can be solved analytically to give

$$\text{Re}[\Pi(q, \omega)] = \begin{cases} \frac{1}{\pi v^2} [\mu_+ + \mu_- + \Lambda_1^{[1,1,-1,-1]}(q, \omega, \mu_+, \mu_-) + 4\zeta_1(q, \omega)] & : 1A \\ \frac{1}{\pi v^2} (\mu_+ + \mu_-) & : 2A \\ \frac{1}{\pi v^2} [\mu_+ + \mu_- + \Lambda_1^{[1,1,1,-1]}(q, \omega, \mu_+, \mu_-) + 2\zeta_1(q, \omega)] & : 1B \\ \frac{1}{\pi v^2} [\mu_+ + \mu_- + \Lambda_1^{[1,1,0,-1]}(q, \omega, \mu_+, \mu_-) + 3\zeta_1(q, \omega)] & : 2B \\ \frac{1}{\pi v^2} [\mu_+ + \mu_- + \Lambda_2^{[0,0,1,0]}(q, \omega, \mu_+, \mu_-) + \frac{1}{2}\zeta_2(q, \omega)] & : 3B \\ \frac{1}{\pi v^2} [\mu_+ + \mu_- + \Lambda_2^{[1,0,1,0]}(q, \omega, \mu_+, \mu_-) + \zeta_2(q, \omega)] & : 4B \\ \frac{1}{\pi v^2} [\mu_+ + \mu_- + \Lambda_1^{[1,1,1,-1]}(q, \omega, \mu_+, \mu_-)] & : 1C \\ \frac{1}{\pi v^2} [\mu_+ + \mu_- + \Lambda_1^{[1,1,1,0]}(q, \omega, \mu_+, \mu_-) + \zeta_1(q, \omega)] & : 2C \\ \frac{1}{\pi v^2} [\mu_+ + \mu_- + \Lambda_1^{[1,1,0,0]}(q, \omega, \mu_+, \mu_-) + 2\zeta_1(q, \omega)] & : 3C \\ \frac{1}{\pi v^2} [\mu_+ + \mu_- + \Lambda_2^{[0,0,1,1]}(q, \omega, \mu_+, \mu_-) + \zeta_2(q, \omega)] & : 4C \\ \frac{1}{\pi v^2} [\mu_+ + \mu_- + \Lambda_2^{[1,0,1,1]}(q, \omega, \mu_+, \mu_-) + \frac{3}{2}\zeta_2(q, \omega)] & : 5C \\ \frac{1}{\pi v^2} [\mu_+ + \mu_- + \Lambda_2^{[1,1,1,1]}(q, \omega, \mu_+, \mu_-) + 2\zeta_2(q, \omega)] & : 6C. \end{cases} \quad (10)$$

The imaginary part of the polarization function is

$$\text{Im}[\Pi(q, \omega)] = \begin{cases} 0 & : 1A \\ \frac{1}{\pi v^2} \Lambda_3^{[-1,-1,1,1]}(q, \omega, \mu_+, \mu_-) & : 2A \\ \frac{1}{\pi v^2} \zeta_2(q, \omega) & : 1B \\ \frac{1}{\pi v^2} [\Lambda_2^{[0,0,1,0]}(q, \omega, \mu_+, \mu_-) + \frac{1}{2}\zeta_2(q, \omega)] & : 2B \\ \frac{1}{\pi v^2} \Lambda_3^{[-1,-1,0,1]}(q, \omega, \mu_+, \mu_-) & : 3B \\ \frac{1}{\pi v^2} \Lambda_3^{[0,-1,0,1]}(q, \omega, \mu_+, \mu_-) & : 4B \\ \frac{1}{\pi v^2} 2\zeta_2(q, \omega) & : 1C \\ \frac{1}{\pi v^2} [\Lambda_2^{[0,0,0,1]}(q, \omega, \mu_+, \mu_-) + \frac{3}{2}\zeta_2(q, \omega)] & : 2C \\ \frac{1}{\pi v^2} [\Lambda_2^{[0,0,1,1]}(q, \omega, \mu_+, \mu_-) + \zeta_2(q, \omega)] & : 3C \\ \frac{1}{\pi v^2} \Lambda_3^{[-1,-1,0,0]}(q, \omega, \mu_+, \mu_-) & : 4C \\ \frac{1}{\pi v^2} \Lambda_3^{[0,-1,0,0]}(q, \omega, \mu_+, \mu_-) & : 5C \\ 0 & : 6C, \end{cases} \quad (11)$$

where we have used the definitions

$$\Lambda_n^{[m_1, m_2, m_3, m_4]}(q, \omega, \mu_+, \mu_-) = -\frac{1}{8\sqrt{|\omega^2 - (vq)^2|}} [m_1 f_n(q, \omega, \mu_+) + m_2 f_n(q, \omega, \mu_-) + m_3 f_n(q, -\omega, \mu_+) + m_4 f_n(q, -\omega, \mu_-)], \quad (12)$$

where

$$f_1(q, \omega, \mu) = (2\mu + \omega)\sqrt{(2\mu + \omega)^2 - (vq)^2} - (vq)^2 \ln \frac{\sqrt{(2\mu + \omega)^2 - (vq)^2} + 2\mu + \omega}{|\sqrt{\omega^2 - (vq)^2} + \omega|},$$

$$f_2(q, \omega, \mu) = (2\mu + \omega)\sqrt{(vq)^2 - (2\mu + \omega)^2} + (vq)^2 \sin^{-1} \frac{2\mu + \omega}{vq},$$

$$f_3(q, \omega, \mu) = (2\mu + \omega)\sqrt{(2\mu + \omega)^2 - (vq)^2} - (vq)^2 \ln \frac{\sqrt{(2\mu + \omega)^2 - (vq)^2} + 2\mu + \omega}{vq}, \quad (13)$$

and

$$\zeta_1(q, \omega) = -\frac{1}{8\sqrt{\omega^2 - (vq)^2}} (vq)^2 \ln \frac{\omega - \sqrt{\omega^2 - (vq)^2}}{vq},$$

$$\zeta_2(q, \omega) = \frac{\pi (vq)^2}{8\sqrt{|\omega^2 - (vq)^2|}}. \quad (14)$$

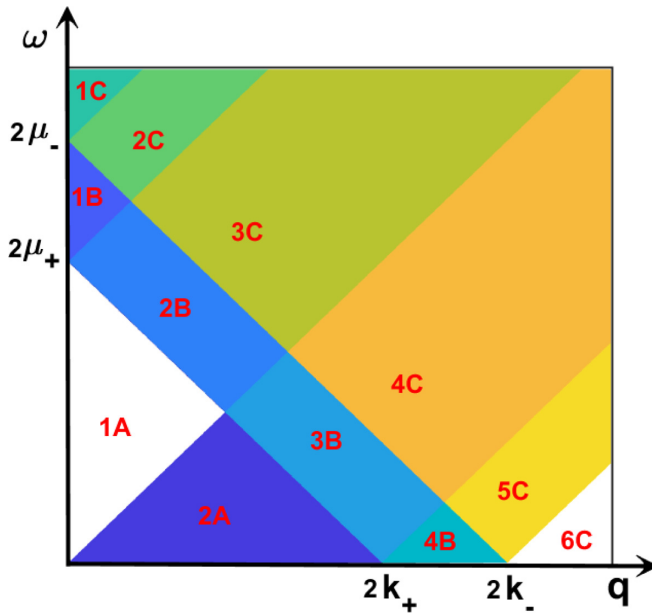


FIG. 3. Regions for the BTBG bands in which the polarization function has different expressions. Here, the Fermi energy is located at $\mu = \Delta_z/12$.

The regions specified in Eqs. (10) and (11) are given by

$$\begin{aligned}
 1A : & \quad \Theta[v(2k_1 - q) - \omega]\Theta[\omega - vq], \\
 2A : & \quad \Theta[v(2k_1 - q) - \omega]\Theta[vq - \omega], \\
 1B : & \quad \Theta[\omega - v(q + 2k_1)]\Theta[v(2k_2 - q) - \omega], \\
 2B : & \quad \Theta[v(q + 2k_1) - \omega]\Theta[\omega - v(2k_1 - q)] \\
 & \quad \times \Theta[v(2k_2 - q) - \omega]\Theta[\omega - vq], \\
 3B : & \quad \Theta[\omega - v(2k_1 - q)]\Theta[v(2k_2 - q) - \omega] \\
 & \quad \times \Theta[vq - \omega]\Theta[\omega - v(q - 2k_1)], \\
 4aB : & \quad \Theta[v(q - 2k_1) - \omega]\Theta[v(2k_2 - q) - \omega], \\
 1C : & \quad \Theta[\omega - v(q + 2k_2)], \\
 2C : & \quad \Theta[v(q + 2k_2) - \omega]\Theta[\omega - v(q + 2k_1)] \\
 & \quad \times \Theta[\omega - v(2k_2 - q)], \\
 3C : & \quad \Theta[v(q + 2k_1) - \omega]\Theta[\omega - v(2k_2 - q)] \\
 & \quad \times \Theta[\omega - vq], \\
 4C : & \quad \Theta[\omega - v(2k_2 - q)]\Theta[vq - \omega] \\
 & \quad \times \Theta[\omega - v(q - 2k_1)], \\
 5C : & \quad \Theta[\omega - v(2k_2 - q)]\Theta[v(q - 2k_1) - \omega] \\
 & \quad \times \Theta[\omega - v(q - 2k_2)], \\
 6C : & \quad \Theta[v(q - 2k_2) - \omega],
 \end{aligned} \tag{15}$$

where $\Theta[\dots]$ represent step functions. The regions given by Eq. (15) are shown in Fig. 3 for the Fermi energy located at $\mu = \Delta_z/12$. As we can see in Eq. (11), the imaginary part of the polarization function $\text{Im}[\Pi(q, \omega)] = 0$, in the white space of Fig. 3 (region 1A and 6C). The white space in Fig. 3 corresponds to values of q and ω for which there is no damping of a collective charge oscillation (undamped

plasmon). The other regions in Fig. 3 ($\text{Im}[\Pi(q, \omega)] \neq 0$) correspond to regions in which collective oscillations are damped (damped plasmon). In Fig. 3, we only plot the regions for a specific Fermi energy $\mu = \Delta_z/12$. When the Fermi energy μ is increased, the value of $\mu_+ = |\mu - \Delta_z/2|$ decreases and the zero imaginary polarization region (1A white region shown in Fig. 3) will shrink. When μ increases to $\Delta_z/2$, the 1A white region shown in Fig. 3 will vanish. As μ further increases to the regime $\mu > \Delta_z/2$, the 1A white region shown in Fig. 3 will reoccur, and the undamped plasmonic wave can be excited in this white region ($\text{Im}[\Pi(q, \omega)] = 0$) again.

As a significant consequence of the dielectric function, we calculate the long-wavelength plasmon dispersion for BTBG by using the above results [Eq. (10) (1A)]. In the long-wavelength limit $q \rightarrow 0^+$, we have the following limiting forms in the low-frequency regimes:

$$\begin{aligned}
 \text{Re}[\Pi(q \rightarrow 0^+, \omega)] & = \frac{q^2}{4\pi\omega^2} \left[\mu_+ + \mu_- - \frac{\omega^2}{4} \left(\frac{1}{\mu_+} + \frac{1}{\mu_-} \right) \right] \\
 & = \begin{cases} \frac{q^2}{4\pi\omega^2} \left[\Delta_z - \omega^2 \left(\frac{\Delta_z}{\Delta_z^2 - 4\mu^2} \right) \right] & : \mu < \frac{\Delta_z}{2}, \\ \frac{q^2}{4\pi\omega^2} \left[2\mu - \omega^2 \left(\frac{\Delta_z}{4\mu^2 - \Delta_z^2} \right) \right] & : \mu > \frac{\Delta_z}{2}. \end{cases} \tag{16}
 \end{aligned}$$

By substituting Eq. (16) into Eq. (7), we get the long-wavelength ($q \rightarrow 0^+$) plasmon mode dispersion for BTBG as

$$q = \begin{cases} \frac{8\pi\epsilon_0\epsilon_r}{e^2} \frac{1}{\Delta_z} \frac{\omega^2}{1 - \frac{\omega^2}{\Delta_z^2 - 4\mu^2}} \approx \frac{8\pi\epsilon_0\epsilon_r}{e^2} \frac{1}{\Delta_z} \omega^2 & : \mu < \frac{\Delta_z}{2}, \\ \frac{8\pi\epsilon_0\epsilon_r}{e^2} \frac{1}{2\mu} \frac{\omega^2}{1 + \frac{\omega^2}{\Delta_z^2 - 4\mu^2}} \approx \frac{8\pi\epsilon_0\epsilon_r}{e^2} \frac{1}{2\mu} \omega^2 & : \mu > \frac{\Delta_z}{2}. \end{cases} \tag{17}$$

In low-frequency ($\omega \ll 1$ eV) regime, the plasmon branch obtained by using the RPA model [shown in Eq. (16)] is in agreement with the plasmon dispersion obtained by using the Lindhard model [shown in Eq. (17)]. All these results [Eqs. (8) and (16)] indicate that the long-wavelength plasmon dispersion is independent of carrier concentration (n) when the Fermi energy was located in the regime $\mu < \Delta_z/2$. This is very different from the 2D plasmon behavior in conventional 2DEG and graphene, where $\omega \propto n^{1/2} \sqrt{q}$ and $\omega \propto n^{1/4} \sqrt{q}$.

$\text{Re}[\Pi(q, \omega)]$ is plotted in Fig. 4(a) for $\theta = 3.89^\circ$, $\Delta_z = 0.06$ eV, and $\mu = 0.01$ eV (the Fermi energy μ is located in the regime $\mu < \Delta_z/2$). Several frequency cuts of Fig. 4(a) are shown in Fig. 4(c). Plots of $\text{Im}[\Pi(q, \omega)]$ can be seen in Fig. 4(b) with θ , Δ_z , and μ chosen to correspond with Fig. 4(a). While the imaginary part of the polarization determines the damping of the plasmon, the real part of the dynamical polarization comes in to determine the location of the plasmon branch in (q, ω) space. The undamped plasmon branch can be obtained by finding the zeros of the dielectric function $\epsilon(q, \omega)$. In the 1A white zero space ($\text{Im}[\Pi(q, \omega)] = 0$) shown in Figs. 3 and 4(b), it is sufficient to solve Eq. (7) to get the plasmon branch. Therefore, we plot the polarization function $\text{Re}[\Pi(q, \omega)]$ and $\text{Im}[\Pi(q, \omega)]$ in Figs. 4(c) and 4(d) for a constant frequency corresponding to three frequency values, $\omega = 5$ (blue line), 25 (red line), and 45 (black line) meV shown in Figs. 4(a) and 4(b). The solutions of Eq. (7) are given by the intersection of the

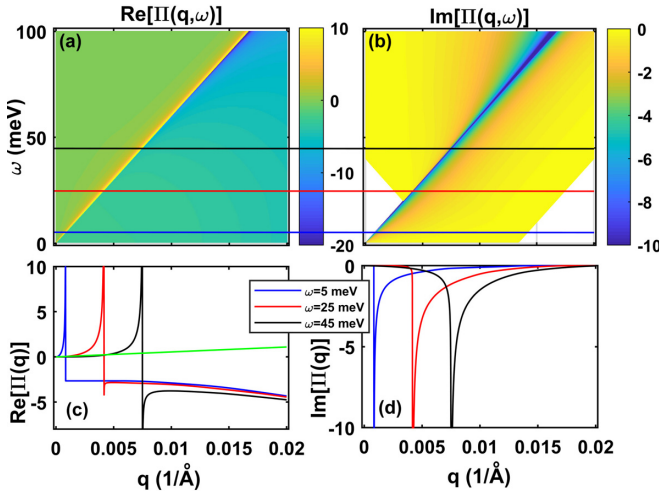


FIG. 4. (a) Real part of the polarization function for $\theta = 3.89^\circ$, $\Delta_z = 0.06$ eV, and $\mu = 0.01$ eV. (b) Imaginary part of the polarization function for θ , Δ_z , and μ chosen to correspond to (a). (c) and (d) are the constant frequency cuts of the real and imaginary parts of the polarization function as a function of q . The blue, red, and black lines in (c) and (d) correspond to the constant frequencies $\omega = 5$ meV, $\omega = 25$ meV, and $\omega = 45$ meV, which are also indicated by the red, blue, and black lines shown in (a) and (b).

$\text{Re}[\Pi(q, \omega)]$ vs $2\epsilon_0\epsilon_r q/e^2$ slope (solid green line) shown in Fig. 4(c). As we can see in Fig. 4(c), the green slope line intersects every function ($\text{Re}[\Pi(q, \omega = 5, 25, 45 \text{ meV})]$) two times and, therefore, there are two solutions at those frequencies ($\omega = 5, 25, 45$ meV). However, the excited plasmonic wave is undamped, only when (q, ω) is located in region 1A ($\text{Im}[\Pi(q, \omega)] = 0$). Therefore, in Fig. 4(c), only the first intersection between the green slope with the blue and red lines corresponds to the undamped plasmon modes.

From an experimental perspective, plasmons appear as resonance peaks in the momentum-resolved electron energy loss spectrum, which directly measures the loss function: $-\text{Im}[1/\Pi(q, \omega)]$. Based on the above polarization function formula [Eqs. (10) and (11)], we calculate the energy loss function ($-\text{Im}[1/\Pi(q, \omega)]$) and display the results in Fig. 5. As we can see in Fig. 5, the energy loss peak (blue) calculated by Eqs. (10) and (11) (RPA deduced formula) is in good agreement with the plasmon spectrum (red solid line) calculated by using Eq. (8) (the long-wavelength plasmon spectrum deduced by using the Lindhard model) in the small (q, ω) regime ($q < 10^{-3}/\text{\AA}$, $\omega < 10$ meV). Therefore, the resonance peaks in the momentum-resolved electron energy loss spectrum shown in Figs. 5(a)–5(c) reconfirm the significant result: When the Fermi energy is located in the regime $\mu < \Delta_z/2$, the long-wavelength plasmon spectrum ($\omega \propto \sqrt{\Delta_z}\sqrt{q}$) is independent of carrier concentration (n) and also does not rely on the specific value of the Fermi energy μ .

C. Finite-range interaction effect

The above analysis for BTBG plasmon dispersion is based on Eq. (3), where we take the electronic interaction $V(r)$ as the long-range Coulomb form $V(r) = \frac{e^2}{4\pi\epsilon_0\epsilon_r r}$, and $V(q) = \frac{e^2}{2\epsilon_0\epsilon_r}$

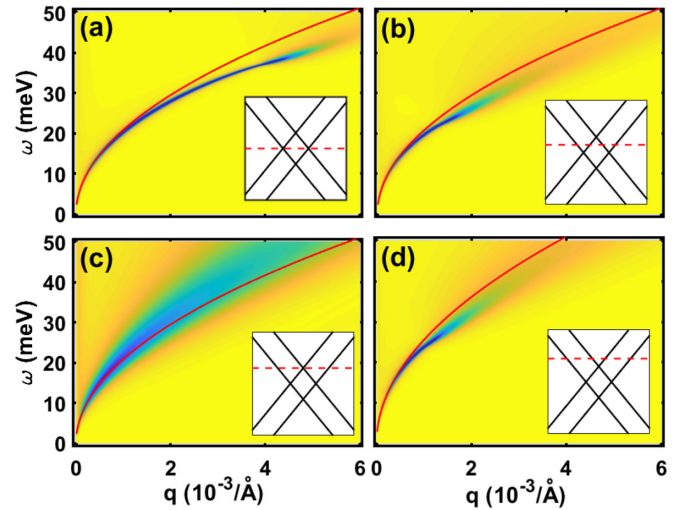


FIG. 5. Energy loss function calculated by RPA results [Eqs. (10) and (11)] for $\theta = 3.89^\circ$, $\Delta_z = 0.06$ eV, and Fermi energy located at (a) $\mu = 0$ meV, (b) $\mu = 15$ meV, (c) $\mu = 30$ meV, and (d) $\mu = 45$ meV. The red solid line is the plasmon spectrum calculated by using the Lindhard model obtained long-wavelength plasmon formula [Eq. (8)]. The inset displays the band structure, and the corresponding Fermi energy indicated by the red dashed line.

is the corresponding Fourier transform. However, in actual one- [32] or two-dimensional materials [33], the polarizable background leads to a screened finite-range interaction. In two-dimensional materials, the impact of a finite-range interaction can be described by replacing the long-range $1/r$ Coulomb interaction with the 2D Keldysh potential [34,35] or Yukawa interaction [36]. Here, for simplicity, we choose the Yukawa interaction,

$$V(r) = \frac{e^2}{4\pi\epsilon_0\epsilon_r} \frac{e^{-\gamma r}}{r}, \quad V(q) = \frac{e^2}{2\epsilon_0\epsilon_r} \frac{1}{\sqrt{q^2 + \gamma^2}}, \quad (18)$$

which has a screening parameter γ , and $V(q)$ is the corresponding Fourier transform of $V(r)$. As we can see, in the $\gamma \rightarrow 0$ limit the interaction reduces to the long-range Coulomb interaction, while at $\gamma \rightarrow \infty$ it approximates the properties of a hard-sphere interaction. The finite screening parameter γ can also be regarded as a Thomas-Fermi wave vector [36]. In BTBG, we obtain the screening parameter γ (Thomas-Fermi wave vector) as

$$\gamma = \frac{e^2}{2\epsilon_0\epsilon_r} \Pi(q \rightarrow 0, \omega = 0) = \frac{e^2}{2\epsilon_0\epsilon_r} \frac{\Delta_z}{\pi v^2}, \quad (19)$$

where the polarizability [$\Pi(q \rightarrow 0, \omega = 0)$] is independent of carrier concentration (n). Clearly, within this approximation the impurity potential is completely screened out within a distance of the order of the inverse of Thomas-Fermi wave vector γ .

Therefore, the long-wavelength plasmon dispersion under a finite-range interaction is of the form

$$\omega = \sqrt{\frac{e^2}{2\epsilon_0\epsilon_r} \frac{\Delta_z}{4\pi} \frac{q}{[q^2 + (\frac{e^2}{2\epsilon_0\epsilon_r} \frac{\Delta_z}{\pi v^2})^2]^{1/4}}} \approx \frac{1}{\sqrt{2}} v q. \quad (20)$$

As we can see in the equation, although the finite-range interaction leads to a linear plasmon dispersion ($\omega \propto q$), the plasmon energy is still independent of the carrier concentration (n).

IV. CONCLUSION

We investigate the dynamical dielectric function of biased twisted bilayer graphene (BTBG) within the random phase approximation (RPA). We find that the perpendicular electric field can remove the degeneration of the graphene Dirac cone and give rise to a Dirac energy difference Δ_z between the two Dirac points at the same valley. When the Fermi energy μ (which is decided by the carrier concentration n)

is located in the regime $\mu < \Delta_z/2$, we surprisingly find that the long-wavelength plasmon dispersion is independent of carrier concentration (n) and also does not rely on the specific value of the Fermi energy (μ). The long-wavelength plasmon dispersion in this regime ($\mu < \Delta_z/2$) can be described by a simple formula, $\omega = \sqrt{\frac{e^2}{8\pi\epsilon_0\epsilon_r}}\sqrt{\Delta_z}\sqrt{q}$. When we take the finite-range interaction into account, the long-wavelength plasmon dispersion is still independent of carrier concentration (n).

ACKNOWLEDGMENT

I thank Zhimin Ji for an interesting discussion about the two-dimensional plasmon in biased twisted bilayer graphene.

APPENDIX

Here, we use the Lindhard model to derive the long-wavelength polarizability $\text{Re } \Pi(q \rightarrow 0^+, \omega)$ and plasmon spectrum for biased twisted bilayer graphene (BTBG).

Since the deviated double Dirac cone [blue and red cone shown in Fig. 1(b)] is decoupled, we can obtain the polarizability for a different Dirac cone $\Pi^\pm(q, \omega)$ separately and the total polarization function can be written as $\Pi(q, \omega) = \Pi^+(q, \omega) + \Pi^-(q, \omega)$. Due to the electron-hole symmetry in each Dirac cone system, the polarization function for the Fermi energy located above or lower than the Dirac points shows the same dynamics. Here, we only deduce one Dirac cone contributed polarizability, which is a function of μ_+ (defined in the main text) for the upper Dirac cone. We can easily get the polarizability for the lower Dirac cone by substituting μ_+ with μ_- . Under a long-wavelength limit $q \rightarrow 0^+$, the Lindhard model shown in Eq. (5) can be simplified to

$$\begin{aligned} \Pi^+(q \rightarrow 0^+, \omega) &= \frac{1}{4\pi^2} \int d^2k \frac{-\mathbf{q} \cdot \nabla f[E(\mathbf{k})]}{\omega - \mathbf{q} \cdot \nabla E(\mathbf{k})} \\ &= -\frac{1}{4\pi^2\omega} \int d^2k \left\{ \left(q_x \frac{\partial f[E(\mathbf{k})]}{\partial k_x} + q_y \frac{\partial f[E(\mathbf{k})]}{\partial k_y} \right) + \frac{v}{\omega} \left(q_x \frac{k_x}{k} + q_y \frac{k_y}{k} \right) \left(q_x \frac{\partial f[E(\mathbf{k})]}{\partial k_x} + q_y \frac{\partial f[E(\mathbf{k})]}{\partial k_y} \right) \right\}. \end{aligned} \quad (\text{A1})$$

In above equation, we have

$$\int d^2k \dots \frac{\partial f[E(\mathbf{k})]}{\partial k_x} = \int d^2k \dots \frac{\partial f[E(\mathbf{k})]}{\partial E(\mathbf{k})} \frac{\partial E(\mathbf{k})}{\partial k_x} = \int d^2k \dots \delta[\mu_+ - vk] \frac{k_x}{k} = \int_0^\infty \delta[\mu_+ - vk] k dk \int_0^{2\pi} d\theta \dots \cos \theta \quad (\text{A2})$$

and

$$\int d^2k \dots \frac{\partial f[E(\mathbf{k})]}{\partial k_y} = \int_0^\infty \delta[\mu_+ - vk] k dk \int_0^{2\pi} d\theta \dots \sin \theta. \quad (\text{A3})$$

By substituting Eqs. (19) and (20) into Eq. (18), we find that the first term shown in Eq. (18) equals zero, $\int d^2k (q_x \frac{\partial f[E(\mathbf{k})]}{\partial k_x} + q_y \frac{\partial f[E(\mathbf{k})]}{\partial k_y}) = 0$, and the integrate result is

$$\Pi^+(q \rightarrow 0^+, \omega) = \frac{q^2}{4\pi\omega^2} \mu_+. \quad (\text{A4})$$

By substituting μ_+ with μ_- , we get

$$\Pi(q \rightarrow 0^+, \omega) = \frac{q^2}{4\pi\omega^2} (\mu_+ + \mu_-) = \frac{q^2}{4\pi\omega^2} \Delta_z. \quad (\text{A5})$$

[1] M. Pletyukhov and V. Gritsev, *Phys. Rev. B* **74**, 045307 (2006).
 [2] C. A. Ullrich and M. E. Flatté, *Phys. Rev. B* **68**, 235310 (2003).
 [3] J. Schliemann, *Phys. Rev. B* **74**, 045214 (2006).
 [4] K. N. A. Grigorenko and M. Polini, *Nat. Photonics* **6**, 749 (2012).

[5] M. Benaissa, W. Sigle, M. Korytov, J. Brault, P. Vennéguès, and P. A. van Aken, *Appl. Phys. Lett.* **103**, 021901 (2013).
 [6] R. H. Ritchie, *Phys. Rev.* **106**, 874 (1957).
 [7] R. A. Ferrell, *Phys. Rev.* **111**, 1214 (1958).
 [8] F. Stern, *Phys. Rev. Lett.* **18**, 546 (1967).

- [9] C. C. Grimes and G. Adams, *Phys. Rev. Lett.* **36**, 145 (1976).
- [10] M.-T. Bootsmann, C.-M. Hu, C. Heyn, D. Heitmann, and C. Schüller, *Phys. Rev. B* **67**, 121309(R) (2003).
- [11] M.-I. Ke, D. Westwood, R. H. Williams, and M. J. Godfrey, *Phys. Rev. B* **51**, 5038 (1995).
- [12] J. Seidel, F. I. Baida, L. Bischoff, B. Guizal, S. Grafström, D. Van Labeke, and L. M. Eng, *Phys. Rev. B* **69**, 121405(R) (2004).
- [13] K. Seal, D. A. Genov, A. K. Sarychev, H. Noh, V. M. Shalaev, Z. C. Ying, X. Zhang, and H. Cao, *Phys. Rev. Lett.* **97**, 206103 (2006).
- [14] V. N. Konopsky and E. V. Alieva, *Phys. Rev. Lett.* **97**, 253904 (2006).
- [15] W. H. Weber, *Phys. Rev. Lett.* **39**, 153 (1977).
- [16] V. I. Safarov, V. A. Kosobukin, C. Hermann, G. Lampel, J. Peretti, and C. Marlière, *Phys. Rev. Lett.* **73**, 3584 (1994).
- [17] A. H. Castro Neto, F. Guinea, N. M. R. Peres, K. S. Novoselov, and A. K. Geim, *Rev. Mod. Phys.* **81**, 109 (2009).
- [18] E. H. Hwang and S. Das Sarma, *Phys. Rev. B* **75**, 205418 (2007).
- [19] V. W. Brar, S. Wickenburg, M. Panlasigui, C.-H. Park, T. O. Wehling, Y. Zhang, R. Decker, C. Girit, A. V. Balatsky, S. G. Louie, A. Zettl, and M. F. Crommie, *Phys. Rev. Lett.* **104**, 036805 (2010).
- [20] A. Scholz, T. Stauber, and J. Schliemann, *Phys. Rev. B* **88**, 035135 (2013).
- [21] C. J. Tabert and E. J. Nicol, *Phys. Rev. B* **89**, 195410 (2014).
- [22] F. Guinea and N. R. Walet, *Proc. Natl. Acad. Sci. USA* **115**, 13174 (2018).
- [23] G. Tarnopolsky, A. J. Kruchkov, and A. Vishwanath, *Phys. Rev. Lett.* **122**, 106405 (2019).
- [24] F. Hu, S. R. Das, Y. Luan, T.-F. Chung, Y. P. Chen, and Z. Fei, *Phys. Rev. Lett.* **119**, 247402 (2017).
- [25] P. Novelli, I. Torre, F. H. L. Koppens, F. Taddei, and M. Polini, *Phys. Rev. B* **102**, 125403 (2020).
- [26] L. Brey, T. Stauber, T. Slipchenko, and L. Martín-Moreno, *Phys. Rev. Lett.* **125**, 256804 (2020).
- [27] C. Lewandowski and L. Levitov, *Proc. Natl. Acad. Sci. USA* **116**, 20869 (2019).
- [28] J. M. Pizarro, M. Rösner, R. Thomale, R. Valentí, and T. O. Wehling, *Phys. Rev. B* **100**, 161102(R) (2019).
- [29] R. Bistritzer and A. H. MacDonald, *Proc. Natl. Acad. Sci. USA* **108**, 12233 (2011).
- [30] J. M. B. Lopes dos Santos, N. M. R. Peres, and A. H. Castro Neto, *Phys. Rev. Lett.* **99**, 256802 (2007).
- [31] N. N. T. Nam and M. Koshino, *Phys. Rev. B* **96**, 075311 (2017).
- [32] R. Egger and H. Grabert, *Phys. Rev. Lett.* **79**, 3463 (1997).
- [33] F. Stern and W. E. Howard, *Phys. Rev.* **163**, 816 (1967).
- [34] L. V. Keldysh, *Pis'ma Zh. Eksp. Teor. Fiz.* **29**, 716 (1979) [*JETP Lett.* **29**, 658 (1979)].
- [35] P. Cudazzo, I. V. Tokatly, and A. Rubio, *Phys. Rev. B* **84**, 085406 (2011).
- [36] G. F. Giuliani and G. Vignale, *Quantum Theory of the Electron Liquid* (Cambridge University Press, Cambridge, U.K., 2005).